Open Archive Toulouse Archive Ouverte (OATAO)

OATAO is an open access repository that collects the work of Toulouse researchers and makes it freely available over the web where possible.

This is an author-deposited version published in: http://oatao.univ-toulouse.fr/
Eprints ID: 13651

To link to this article: DOI: 10.2514/1.J053507
URL: http://dx.doi.org/10.2514/1.J053507

To cite this version: Jardin, Thierry and Grondin, Gilles and Gressier, Jérémie and Huo, Chao and Doué, Nicolas and Barènes, Roger *Revisiting Froude's Theory for Hovering Shrouded Rotor.* (2015) AIAA Journal. ISSN 0001-1452

Any correspondence concerning this service should be sent to the repository administrator: staff-oatao@inp-toulouse.fr

Revisiting Froude's Theory for Hovering Shrouded Rotor

T. Jardin,* G. Grondin,* J. Gressier,† C. Huo,‡ N. Doué,§ and R. Barènes*
University of Toulouse, 31055 Toulouse, France

DOI: 10.2514/1.J053507

This paper extends Froude's momentum theory for free propellers to the analysis of shrouded rotors. A one-dimensional analytical approach is provided, and a homokinetic normal inlet surface model is proposed. Formulations of thrusts and power for each system component are derived, leading to the definition of optimum design criteria and providing insight into the global aerodynamics of shrouded rotors. In the context of micro-air vehicles applications, assessment of the model is conducted with respect to numerical data. Overall, comparison between numerical and analytical results shows good agreement and highlights the sensitivity of the model to viscous effects.

Nomenclature

A_1	=	inlet surface area for momentum (balance), m^2
A_1'	=	inlet surface area for mass flow rate, m^2
A_2	=	outlet surface area, m^2
A_R	=	rotor surface area, m^2
D_R	=	rotor diameter, m
K_1	=	A_1/A_R ratio
K_1'	=	A_1'/A_R ratio
K_2	=	A_2/A_R ratio
k	=	A_1'/A_1 ratio
L_S	=	shroud length, m
$\dot{m}$	=	mass flow rate, kg/s
$\boldsymbol{n}$	=	surface normal unit vector
p	=	static pressure, Pa
p_t	=	total pressure, Pa
p_1	=	inlet static pressure, Pa
p_2	=	outlet static pressure, Pa
p_∞	=	farfield static pressure, Pa
Δp	=	pressure jump at actuator disk, Pa
P_i	=	induced power, W
R_R	=	rotor radius, M
S_1	=	inlet surface
S_2	=	outlet surface
S_{R_1}	=	upstream rotor surface
S_{R_2}	=	downstream rotor surface
S_{S_1}	=	upstream shroud (inner) surface
S_{S_2}	=	downstream shroud (inner) surface
T_R	=	rotor thrust, N
T_{S_1}	=	upstream shroud thrust, N
T_{S_2}	=	downstream shroud thrust, N
T_T	=	total thrust, N
v	=	velocity, m/s
v_1	=	velocity at the shroud inlet, m/s
v_2	=	velocity at the shroud outlet, m/s
v_i	=	induced velocity at the rotor, m/s
V_1	=	upstream (control) volume
V_2	=	downstream (control) volume
ρ	=	fluid density, kg/m^3

*Research Scientist, ISAE, Aerodynamics, Energetics and Propulsion Department, 10 Avenue Edouard Belin.
†Associate Professor, ISAE, Aerodynamics, Energetics and Propulsion Department, 10 Avenue Edouard Belin.
‡Ph.D. Student, ISAE, Aerodynamics, Energetics and Propulsion Department, 10 Avenue Edouard Belin.
§Research Engineer, ISAE, Aerodynamics, Energetics and Propulsion Department, 10 Avenue Edouard Belin.

I. Introduction

IN THE past decade, micro-air vehicles (MAVs) have gained interest owing to their ability to perform missions of observation at relatively low cost. Institutional fundings (e.g. 1996–2000 Micro-Air Vehicles Program initiative by the US Defense Advanced Research Projects Agency, DARPA) considerably promoted research dedicated to the development of MAVs, leading to three distinct concepts: fixed-wing, flapping-wing, and rotary-wing MAVs [1–3]. While fixed-wing MAVs have a priori no hovering capabilities (although new concepts tend to achieve horizontal/vertical transition flight), flapping-wing and rotary-wing MAVs may offer the possibility to operate in confined environments. Yet, flapping-wing MAVs exhibit both complex mechanics and aerodynamics [4–7], making it an immature technology. Thus, rotary-wing MAVs appear to be the most relevant solution for indoor scene recognition, cave exploration or monuments surveillance.

Rotary-wing MAVs can further be divided into two categories: whether their rotor is free or shrouded. Shrouded-rotors are inherently safe and may enhance aerodynamics performance owing to the lifting property of the shroud and blade-tip vortex annihilation, specifically under hovering conditions [8,9]. Although such configurations may suit missions of observation in confined environments, they remain poorly documented and no universal guidelines have emerged for the design of efficient shrouded-rotors at MAV scale.

Pereira and Chopra [9,10] explored the influence of some design parameters on aerodynamics performance of a hovering single shrouded rotor at MAV scale. Overall, the authors have experimentally demonstrated the sensitivity of the total thrust coefficient, at a given power coefficient, to diffuser divergence angle, diffuser length, inlet lip radius and blade tip clearance. Lakshminarayan and Baeder [11] have extended these investigations using a numerical approach, further revealing the influence of inlet shape on the global performance of the single shrouded rotor. Similarly, Lee et al. [12] have experimentally investigated the role of rotor-rotor spacing, rotor position, inlet shape and blade tip clearance on the performance characteristics of a coaxial shrouded rotor. Their work not only focuses on hovering flight conditions but also addresses axial climb and edgewise forward flight conditions. Lately, Hrishikeshavan and Chopra [13] analyzed the response of a single shrouded rotor to edgewise gusts.

Rather than resorting to heavy experimental and numerical approaches, analytical approach may, at relatively low cost, provide simple fruitful information on rotor flows, hence setting guidelines for the design of shrouded rotor MAVs [14,15]. Toward that end, the present paper aims at revisiting Froude's theory for shrouded rotors, subsequently leading to the definition of a simple one-dimensional model from which optimal criteria can be derived. Secondly, the model is assessed using numerical data.

II. Analytical Model

In this section, we define a theoretical model for the analysis of shrouded rotors. Figure 1 is an illustration of the associated system.

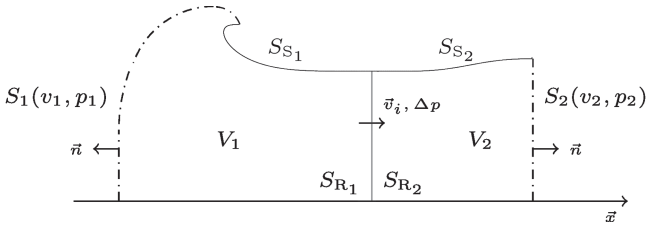

Fig. 1 Scheme of the axisymmetric system illustrating the analytical model.

Surfaces labelled by subscript 1 and 2 delimit the upstream and downstream control volume V_1 and V_2, respectively.

A. Model Definition

Following Froude's theory, the rotor can be approximated by an infinitely thin flat disk (disk actuator). A uniform pressure jump Δp is imposed across the disk, which induces a continuous velocity v_i at the rotor. The left (upflow) and right (downflow) surfaces of the rotor are denoted S_{R_1} and S_{R_2} respectively. This approach, though valid for both single and coaxial rotors, is more consistent with coaxial contra-rotating rotor modeling since swirl effects are omitted.

Conversely to Froude's classical theory, the shroud here introduces a solid boundary, denoted S_{S_1} and S_{S_2} upstream and downstream of the rotor respectively, which constrains the fluid flow. S_1 and S_2 stand for the inlet and exit surfaces of the system respectively.

The flow is assumed to be steady, incompressible and non-viscous with an ambient pressure p_∞. The total and static pressures (p_t and p respectively) upstream of the rotor (i.e. within V_1) are given by

$$p_t = p_\infty \quad \text{and} \quad p = p_\infty - \rho v^2/2 \tag{1}$$

where ρ and v are the local fluid density and velocity. Identically, the total and static pressures downstream of the rotor (i.e. within V_2) are given by

$$p_t = p_\infty + \Delta p \quad \text{and} \quad p = p_\infty + \Delta p - \rho v^2/2 \tag{2}$$

It should be emphasized that the present actuator disk approach considers the rotor (or pair of rotors) as a perfect system. Therefore, the classical figure of merit which usually characterizes rotor quality is here inappropriate. Rather, the model highlights the role of the shroud on the aerodynamics of the whole system by evaluating its ability to convert induced power into thrust.

In what follows, formulations will be derived with respect to hovering conditions [16,17]. Similar formulations for general inflow velocities are addressed in the appendix.

B. Thrust and Power: Dimensional Formulations

As stated in the previous section, the flow is assumed to be steady and non-viscous. In addition, the fluid is assumed to be at rest on the outer region of the shroud, which yields $p = p_\infty$ and $v = 0$ on these outer surfaces, where integrals of $p - p_\infty$ and v will be zero. Thus, forces on the outer shroud surfaces are zero, and forces on both upstream and downstream shroud sections will comprise only the contributions of their respective inner surfaces.

The aerodynamic force experienced by a solid surface S_S of the system can be derived from the momentum balance equation applied over a control volume V of fluid delimited by S_S and fluid surfaces S

$$\boldsymbol{F} = -\int_S ((p - p_\infty)\boldsymbol{n} + \rho(\boldsymbol{v}\cdot\boldsymbol{n})\boldsymbol{v})\,\mathrm{d}s \tag{3}$$

where $\boldsymbol{n}$ is the outward-pointing normal to solid and fluid surfaces. The pressure term is written under its relative form since the integral of the constant ambient pressure on the closed surface $S_S \cup S$ is zero. Note that the formulation is valid only under steady assumptions. Besides, viscous terms are also omitted [18–20].

The system illustrated on Fig. 1 is axisymmetric with respect to the $\boldsymbol{x}$ axis, hence the radial component of the aerodynamic force is null. Therefore, only the thrust T ($\boldsymbol{x}$ component of the aerodynamic force with a positive orientation backwards) is considered

$$T = -\boldsymbol{F}\cdot\boldsymbol{x} = \int_S ((p - p_\infty)n_x + \rho(\boldsymbol{v}\cdot\boldsymbol{n})v_x)\,\mathrm{d}s \tag{4}$$

where n_x and v_x are the projections of $\boldsymbol{n}$ and $\boldsymbol{v}$ on the $\boldsymbol{x}$ axis respectively.

Besides, the mass flow rate $\dot{m}$ through surface S can be introduced as

$$\dot{m} = \int_S \rho(\boldsymbol{v}\cdot\boldsymbol{n})\,\mathrm{d}s \tag{5}$$

If $\boldsymbol{n}$ and $\boldsymbol{v}$ are collinear along the surface S of the control volume V, the previous equations become

$$T = \int_S ((p - p_\infty)n_x + \rho v^2 n_x)\,\mathrm{d}s \tag{6}$$

and

$$\dot{m} = \int_S \rho v\,\mathrm{d}s \tag{7}$$

Furthermore, in the following subsections, surface integration is performed under the assumption that $(p - p_\infty)$ and ρv^2 are uniform along a given surface. This assumption and the $\boldsymbol{n}$ and $\boldsymbol{v}$ collinearity assumption are intrinsic to Froude's theory at the rotor disk surface S_R and are reasonably valid at the exit surface S_2 of the system for a straightened adapted nozzle. They are also reasonably valid at the inlet of the system, along a quasi-homokinetic surface that is normal to local fluid velocity. Such inlet surface will be referred to as S_1. Note that S_1 is depicted on Fig. 1 as a simple illustration. Its precise definition will further be addressed in Sec. III. It should be noted that these assumptions build a one-dimensional model.

Thus, the integration of Eqs. (6) and (7) reduces to the surface integral of n_x and 1, respectively. Two distinct areas can then be associated with a given surface S_i

$$A_i = \int_{S_i} n_x\,\mathrm{d}s \tag{8}$$

and

$$A_i' = \int_{S_i} \mathrm{d}s \tag{9}$$

If the given surface S_i is purely directed along the radial axis, then $A_i = A_i'$. This is the case for the rotor S_R and outlet S_2 surfaces, with corresponding areas A_R and A_2, respectively. On the other hand, A_1 and A_1' need to be distinctly defined for S_1 (as shown in Fig. 2).

Following these definitions, one can then introduce the ratios $K_1 = A_1/A_R$, $K_1' = A_1'/A_R$ and $K_2 = A_2/A_R$. It is emphasized that K_1 can be directly related to the inlet geometry of the shroud while K_1' reflects the aerodynamics of the shroud inlet. For clarity, the ratio $k = K_1'/K_1$ is also introduced. At this point, k can be anticipated to be significantly greater than 1.

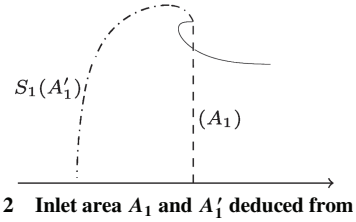

Fig. 2 Inlet area A_1 and A_1' deduced from S_1.

1. Total Thrust

Total thrust can be derived from momentum balance [Eq. (6)] applied over the control volume $V_1 \cup V_2$ enclosing the whole system

$$T_T = \int_{S_1 \cup S_2} ((p - p_\infty) n_x + \rho v^2 n_x) \, \mathrm{d}s \tag{10}$$

Imposing pressure equilibrium at the shroud exit (surface S_2) and substituting Eq. (1) yields

$$T_T = \rho v_2^2 A_2 - \frac{1}{2} \rho v_1^2 A_1 \tag{11}$$

Then, using $\dot{m} = \rho v_1 A_1' = \rho v_2 A_2$ and introducing K_1, K_2 and k, total thrust can be expressed as

$$T_T = \frac{1}{2} \rho A_R \left(\frac{\dot{m}}{\rho A_R} \right)^2 \left(\frac{2}{K_2} - \frac{1}{k^2 K_1} \right) \tag{12}$$

2. Rotor Thrust

Similarly, rotor thrust can be derived from momentum balance [Eq. (6)] applied over the infinitely thin control volume enclosing the actuator disk and delimited by surfaces S_{R_1} and S_{R_2}

$$T_R = \int_{S_{R_1} \cup S_{R_2}} ((p - p_\infty) n_x + \rho v_x^2 n_x) \, \mathrm{d}s \tag{13}$$

The continuity of v_x across the rotor cancels out the integral of $\rho v_x^2 n_x$ term and the pressure step across the rotor yields

$$T_R = A_R \Delta p \tag{14}$$

In addition pressure equilibrium at the shroud exit writes $p_2 = p_\infty$ and from Eq. (2)

$$\Delta p = \rho v_2^2 / 2 \tag{15}$$

Hence, substituting Eq. (15) into (14) brings

$$T_R = \frac{1}{2} \rho A_R v_2^2 \tag{16}$$

Then, replacing v_2 by $\dot{m}/\rho A_2$ and introducing K_2, the expression becomes

$$T_R = \frac{1}{2} \rho A_R \left(\frac{\dot{m}}{\rho A_R} \right)^2 \left(\frac{1}{K_2} \right)^2 \tag{17}$$

3. Shroud Thrust

Shroud thrust can simply be expressed as the difference between total thrust and rotor thrust

$$T_S = T_T - T_R = \frac{1}{2} \rho A_R \left(\frac{\dot{m}}{\rho A_R} \right)^2 \left(\frac{2}{K_2} - \frac{1}{k^2 K_1} - \frac{1}{K_2^2} \right) \tag{18}$$

For analysis purposes, it may be convenient to dissociate the thrust generated by the upstream part of the shroud T_{S_1} from that generated by the downstream part T_{S_2}. This can be achieved by applying the momentum balance over the control volumes V_1 and V_2 respectively. Using Eqs. (1), (2), and (15), T_{S_1} and T_{S_2} can be expressed as follows

$$T_{S_1} = \frac{1}{2} \rho A_R \left(\frac{\dot{m}}{\rho A_R} \right)^2 \left(1 - \frac{1}{k^2 K_1} \right) \tag{19}$$

$$T_{S_2} = -\frac{1}{2} \rho A_R \left(\frac{\dot{m}}{\rho A_R} \right)^2 \left(1 - \frac{1}{K_2} \right)^2 \tag{20}$$

4. Induced Power

Expressing induced power P_i as the product between rotor thrust T_R and induced velocity v_i yields

$$P_i = T_R v_i = \frac{1}{2} \rho A_R \left(\frac{\dot{m}}{\rho A_R} \right)^3 \left(\frac{1}{K_2} \right)^2 \tag{21}$$

From the designer's perspective, it is convenient to express induced power as a function of the total force. Indeed, the design of a MAV usually requires the total force as an input parameter, the total mass to be lifted being in most cases predefined. Thus, substituting Eq. (12) into Eq. (21) brings

$$P_i = \frac{1}{2} \rho A_R \left(\frac{1}{K_2} \right)^2 \left(\frac{T_T}{\rho A_R} \left(\frac{1}{K_2} - \frac{1}{2k^2 K_1} \right)^{-1} \right)^{\frac{3}{2}} \tag{22}$$

C. Thrust and Power: Non-Dimensional Formulations

The results defined in the previous section are summarized in Table 1 under their non-dimensional form (labelled with $*$). The non-dimensional forms for thrusts and power are obtained with respect to $\rho A_R v_i^2/2$ and $\rho A_R v_i^3/2$, respectively. The bottom line in Table 1 is the particular case where $k^2 K_1$ approaches ∞. This is relevant due to the (a priori) relatively high value of k. In addition, it shows that the general Froude's momentum theory for free propellers is recovered for $K_2 = 0.5$.

This global overview indicates that, at a given mass flow rate, the upstream shroud thrust is an explicit function of the inlet parameter $k^2 K_1$ while the downstream and rotor thrusts are explicit functions of the outlet ratio K_2. This suggests that the outlet parameter K_2 drives the functioning of the rotor. Such interplay is also visible on the expression of the induced power, highlighting a potential optimisation of the system via an adequate design of the exit nozzle (surface S_2).

It can be observed that T_{S_2} is always negative; i.e. the downstream part of the shroud is always dragging. However, relation (22) shows that increasing that drag can be beneficial to the overall performance, due to the interplay between K_2 and T_R with respect to P_i.

Finally, it can be seen from the specific $k^2 K_1 \to \infty$ case (third row in Table 1) that the shroud thrust is positive if $K_2 > 1/2$, i.e. if the streamtube is expanded with respect to the free (Froude's) streamtube. Conversely, the shroud thrust is negative if $K_2 < 1/2$.

All these straightforward observations indicate that deeper insight can be obtained from the model. This is the scope of the next section.

Table 1 Non-dimensional formulations for thrusts and power

	T_R^*	T_S^*	$T_{S_1}^*$	$T_{S_2}^*$	T_T^*	P_i^*
$(k = K_1'/K_1)$	$(\frac{1}{K_2})^2$	$(\frac{2}{K_2} - \frac{1}{k^2 K_1} - \frac{1}{K_2^2})$	$(1 - \frac{1}{k^2 K_1})$	$-(1 - \frac{1}{K_2})^2$	$(\frac{2}{K_2} - \frac{1}{k^2 K_1})$	$(\frac{1}{K_2})^2$
$(k^2 K_1 \to \infty)$	$(\frac{1}{K_2})^2$	$(\frac{2}{K_2} - \frac{1}{K_2^2})$	1	$-(1 - \frac{1}{K_2})^2$	$(\frac{2}{K_2})$	$(\frac{1}{K_2})^2$

Third row is derived from second row using $k^2 K_1 \to \infty$.

D. Model Characteristics

1. Minimum Induced Power

Figure 3 depicts the induced power P_i as a function of the exit ratio K_2 at given total thrust T_T and inlet ratio k^2K_1 [Eq. (22)]. As an example of MAV application, we consider a rotor of diameter 180 mm with $k^2K_1 = 2$, 20, and ∞ and generating $T_T = 2.5$, 5, and 7.5 N under hovering conditions. Note that the curves for different T_T collapse onto a single curve when P_i is non-dimensionalized due to the self-similarity of the solution.

Interestingly, it is observed that the induced power reaches a global minimum at a specific value of K_2. This simple result suggests that the shroud can be optimized by tuning parameter K_2 in order to modify the relative contribution of the rotor and shroud thrusts with respect to P_i, up to an optimum operating point. In that sense, the derivation of the induced power (at given T_T and k^2K_1) with respect to K_2 may provide an optimum design criterion. From Eq. (22):

$$\frac{\partial P_i}{\partial K_2} = \frac{1}{2}\rho A_R \left(\frac{T_T}{\rho A_R}\right)^{\frac{3}{2}} \times -\frac{3}{2}\left(K_2^{\frac{1}{3}} - \frac{K_2^{\frac{4}{3}}}{2k^2K_1}\right)^{-\frac{5}{2}} \times \left(\frac{1}{3}K_2^{-\frac{2}{3}} - \frac{4}{3}\frac{K_2^{\frac{1}{3}}}{2k^2K_1}\right) \tag{23}$$

Therefore, $\partial P_i/\partial K_2 = 0$ implies

$$\frac{1}{3}K_2^{-\frac{2}{3}} - \frac{4}{3}\frac{K_2^{\frac{1}{3}}}{2k^2K_1} = 0 \tag{24}$$

which yields the optimal value

$$K_2 = k^2K_1/2 \tag{25}$$

This particular value is associated with an optimum mass flow rate $\dot{m}_{\text{opt}}$. The latter can be obtained by substituting the optimum value of K_2 into Eq. (12), which gives

$$\dot{m}_{\text{opt}} = \sqrt{\frac{2}{3}\rho A_R k^2 K_1 T_T} \tag{26}$$

Thus, the geometric parameter K_2 can be viewed as a way to constrain the mass flow rate, up to a specific value that optimizes the shroud performance.

Note that the same result can be obtained by deriving P_i with respect to $\dot{m}$ (see demonstration in the Appendix).

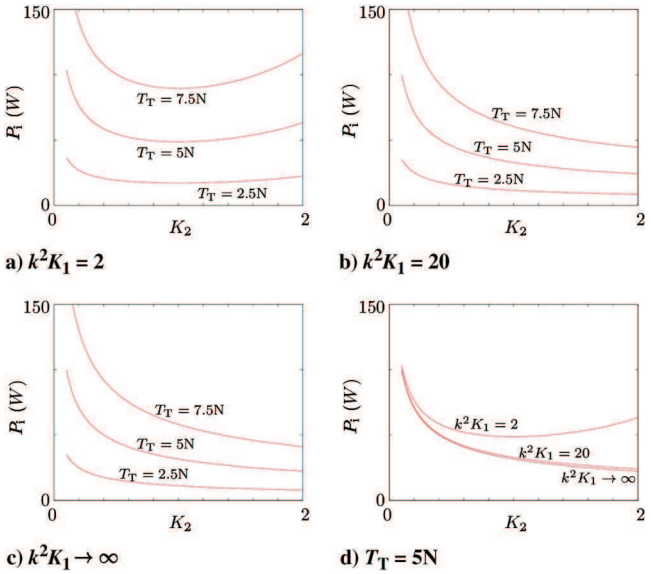

Fig. 3 P_i as a function of K_2 with fixed a-c) k^2K_1 and d) T_T.

2. Shroud Thrust

In order to further investigate the model characteristics, we focus on the thrust generated by the shroud. In particular, attention should be paid to the relative contribution of the upstream and downstream parts of the shroud.

Firstly, the evaluation of the threshold beyond which the shroud produces thrust rather than generates drag can be obtained by writing the following equation:

$$T_S > 0 \tag{27}$$

which using Eq. (18) yields

$$-K_2^2 + 2K_2k^2K_1 - k^2K_1 > 0 \tag{28}$$

Hence, solving for the roots of quadratic Eq. (28) (which admits a solution for $k^2K_1 \geq 1$), the model shows that the shroud produces thrust if

$$k^2K_1 - \sqrt{k^2K_1(k^2K_1 - 1)} < K_2 < k^2K_1 + \sqrt{k^2K_1(k^2K_1 - 1)} \tag{29}$$

It is unlikely that conventional MAV designs reach the upper limit. This is partly due to the nozzle diffusion angle constraint (diffusion angle typically below 10–11 deg [9,17]) that prevents the occurrence of nozzle flow separation and deterioration of the global aerodynamic performance. However, due to the recent extension of MAV's field of application, unconventional designs may emerge. For instance, recent interest in unmanned cave exploration have favored the need for very low aerodynamic footprint MAVs with large diverging exit [21]. On the other hand, the lower limit fixes a design constraint that is much more likely to be violated. Alternatively, Eq. (29) can be reformulated, with $\delta_k = k^2K_1 - 1/2$, to highlight the $K_2 = 1/2$ limit associated with Froude's theory ($k^2K_1 \to \infty$)

$$\frac{1}{2} + \frac{1}{4}\frac{1}{\delta_k + \sqrt{\delta_k^2 - \frac{1}{4}}} < K_2 < \frac{1}{2} + \frac{1}{4}\frac{1}{\delta_k - \sqrt{\delta_k^2 - \frac{1}{4}}} \tag{30}$$

Interestingly, as previously mentioned, a glance at Eq. (20) shows that the downstream part of the shroud is detrimental to thrust production, as T_{S_2} is always negative. Therefore, Eq. (29) defines the thresholds above and below which the upstream thrust more than compensates for the downstream drag (see Fig. 4 for illustration). These observations once again suggest that the primary role of the downstream part of the shroud (or of associated geometric parameter K_2) is not to produce thrust but to drive the mass flow rate up to an optimum value. In that sense, it can also be observed that the downstream drag may be suppressed for $K_2 = 1$, while this value is not optimal in terms of induced power consumption (vertical line marks the optimal K_2 in Fig. 4).

It has been shown that some insights could be obtained from a very simple analysis of the shrouded rotor system. However, as previously introduced, the definition of the inlet surface required to setup the model is not straightforward, the flow being highly distorted (i.e. strongly two-dimensional) at the shroud inlet.

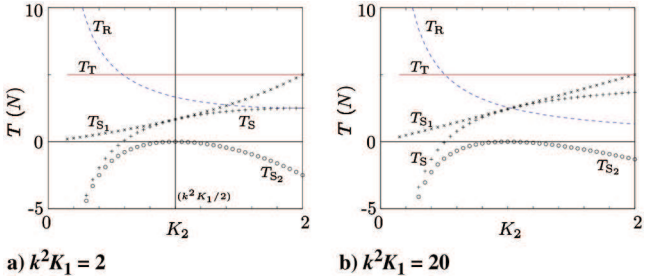

Fig. 4 T_T, T_R, T_S, T_{S_1} and T_{S_2} as a function of K_2.

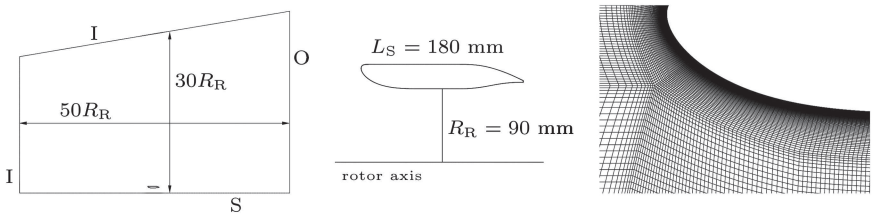

Fig. 5 a) Computational domain, b) shroud geometry, and c) mesh in the vicinity of the lip.

As such, in order to further assess the analytical model and to provide a more thorough definition of the inlet parameter k^2K_1, a numerical approach based on the resolution of the Navier–Stokes equations is conducted in the next section.

III. Numerical Approach

In this section, the shrouded rotor aerodynamics is addressed by means of a numerical approach. The geometry of the shrouded rotor considered here is illustrated in Fig. 5b.

A. Computational Settings

The Navier–Stokes equations are solved using a finite-volume method. Taking advantage of the symmetry of revolution of the system, and given that the Reynolds number based on the rotor induced velocity v_i and rotor diameter D_R is on the order of 200, 000 (Mach number number $\ll 1$), their incompressible, two-dimensional axisymmetric form is considered.

The computational domain is displayed in Fig. 5a. It consists of 130,000 hexahedral cells, refined in the vicinity of the shroud wall (see Fig. 5c). Similarly to the analytical approach, the rotor is modeled as a disk actuator through which a uniform pressure jump Δp is imposed. The shroud surface is modeled as a non-slip wall and is embedded within a large flowfield that extends 50 R_R and 30 R_R in the axial and radial directions respectively. The associated boundaries are subjected to Dirichlet velocity and pressure conditions at the inlet (labelled I on Fig. 5a) and outlet (labelled O on Fig. 5a), respectively.

Both non-viscous (Euler) and viscous computations are performed. For the latter, the turbulence closure is achieved using a realizable k-ϵ model. Mesh refinement in the vicinity of the shroud ensures that y^+ values do not exceed 0.5. The spatial discretisation is achieved using second order schemes. In order to reach a steady solution, transient computations are performed, using first order implicit time formulation. Additional tests have been performed in order to ensure mesh convergence.

B. Numerical Flow Fields

Figure 6a depicts the Euler pressure field induced by the 180 mm diameter shrouded rotor, with exit parameter $K_2 \approx 1.19$. The specific case of a 2.5 N rotor thrust (corresponding to a $\Delta p = 100$ Pa pressure jump) is considered. A pressure discontinuity associated with the actuator disk condition can be clearly observed at the rotor position. While pressure levels downstream of the rotor are only weakly affected, a low pressure region develops upstream of the rotor and extends to the shroud lip. This simple observation corroborates the analytical model in that the shroud thrust seems to be primarily generated by the upstream part of the shroud rather than the downstream part. Furthermore, it emphasizes the role of the shroud lip where a strong suction applies to the wall regions where normal vectors $\boldsymbol{n}$ have a significant x-component.

The correlated velocity flowfield is displayed on Fig. 6b. Although the strongest velocity magnitudes are observed at the rotor location, it can be seen that the velocity flowfield is significantly affected at the shroud lip. In particular, strongly two-dimensional velocity iso-contours highlight the potential issues associated with the $v = C^{\text{st}}$ constraint imposed by the analytical model, and in a more general perspective by one-dimensional approaches. This observation suggests that a definition for the inlet surface of the model is not straightforward. Definition of the inlet surface is the scope of the next section.

Figures 6c and 6d show the viscous flow fields computed for the same configuration. Both pressure and velocity fields are not fundamentally altered with respect to non-viscous computations. The most prominent difference resides in the development of a boundary layer and the diffusion of the shear layer in the wake of the shroud.

C. Definition of the Model's Inlet Parameter (k^2K_1)

In this section a definition for the inlet surface S_1 required to setup the analytical model proposed in Sec. II is given. As previously introduced, S_1 should be defined such that Eqs. (6) and (7) can reasonably be treated under one-dimensional assumptions, despite the two-dimensional nature of the flowfield.

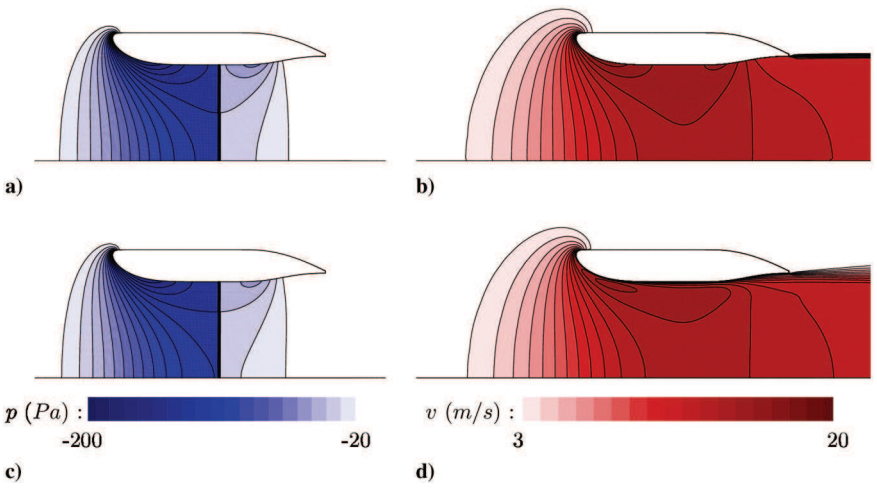

Fig. 6 a, c) Pressure and b, d) velocity magnitudes iso-contours of a, b) Non-viscous (Euler) and c, d) viscous (k-ϵ) computations.

Here, the inlet surface is fixed such that $\boldsymbol{n}$ is collinear to the local fluid velocity. Among the infinite possible surfaces that are locally normal to streamtraces, only one minimizes the average of $|v-\bar{v}|/|\bar{v}|$, where v and $\bar{v}$ are the magnitude and mean value of $\boldsymbol{v}$ along the inlet surface respectively. This particular quasi-homokinetic solution is displayed on Fig. 7 (far-out view of Fig. 6b) together with local velocity vectors. The average of $|v-\bar{v}|/|\bar{v}|$ along this particular solution is on the order of 2.9%, as shown in Fig. 8. Note that $|v-\bar{v}|/|\bar{v}|$ reflects the velocity deviation with respect to a perfectly homokinetic surface. Thus, due to the 2.9% value, the solution is referred to as a 'quasi-homokinetic' surface rather than 'homokinetic surface' (which would imply $|v-\bar{v}|/|\bar{v}|=0$). In this regard, Fig. 8 depicts the value of $|v-\bar{v}|/|\bar{v}|$ computed for multiple inlet surfaces (referred on the abscissa using their K_1' values) that are locally normal to streamtraces. As previously mentioned, we introduce the area of the algebric projection of S_1 onto the radial axis ($A_1=\int_{S_1} n_x ds$) and the area of S_1 ($A_1'=\int_{S_1} \mathrm{d}s$). Given that $\int_\Sigma n_x\,\mathrm{d}s$ is null over any arbitrary closed surface Σ, it can be simply shown that $A_1=\int_{S_1} n_x\,\mathrm{d}s$ is equal to the area of the straight geometric surface that extends from the rotor axis to the external part of the shroud. This makes the value of K_1 rather straightforward.

Hence, the analytical model relies on the inlet parameter k^2K_1, which depends on both areas A_1 and A_1'. This is in contrast with classical one-dimensional approaches for which a single inlet area is used. As previously expressed, one-dimensional assumptions are not strictly valid here if a single inlet area is used. In such cases, k reduces to 1 and the inlet parameter reduces to K_1.

Table 2 shows the analytical value of T_T computed for four distinct inlet parameters. It is compared with the value of T_T obtained from non-viscous (Euler) numerical computations. Note that a unique comparison at $\Delta p=100$ Pa ($T_R=2.5$ N) is conducted since both analytical and numerical non-viscous solutions for T_T are directly proportional to Δp (self-similarity).

The first inlet parameter is based on a single area ($k=1$) obtained from the surface that extends from the rotor axis to the most upstream point of the shroud. The surface is referred to as the 'geometric inlet' and the resulting value of K_1, hence that of k^2K_1, is equal to 1.63. The second inlet parameter is based on the sphere cap model introduced by Dyer [22] and Pereira and Chopra [23] to evaluate the pressure distribution along the shroud via a one-dimensional approach. The surface is a hemisphere that extends from the rotor axis to the most upstream point of the shroud. The resulting value of K_1, hence that of k^2K_1, is equal to 3.27. The third inlet parameter is based on A_1 and A_1' obtained from the homokinetic surface. Here, $K_1=1.78$ and $K_1'=6.80$, which yields $k^2K_1=26$. Finally, the fourth inlet parameter is based on the assumption that the relatively high value of k brings $k^2K_1\to\infty$. The surface is referred to as the 'Froude's inlet'.

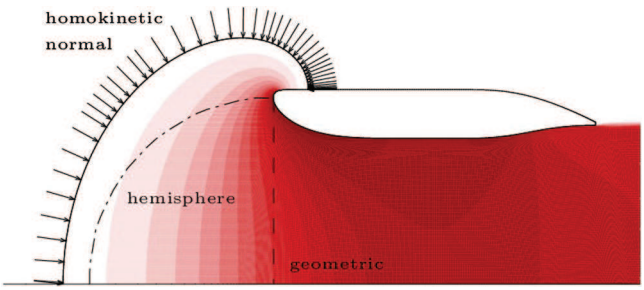

Fig. 7 Velocity flow fields from Non-viscous (Euler) computations and inlet surfaces.

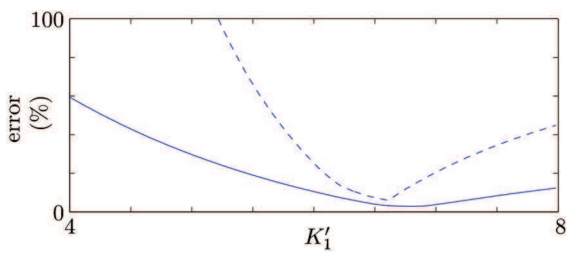

Fig. 8 Average (plain) and maximum (dashed) values of $|v-\bar{v}|/|\bar{v}|$ for several inlet surfaces.

Table 2 Comparison of the analytical value of T_T for distinct inlet surface models

Inlet model	k^2K_1	T_T (N)	Error
Geometric	1.63	3.84	−35.5%
Hemisphere	3.27	4.94	−17%
Homokinetic	26	5.90	−1.0%
Froude's	∞	6.03	+1.3%

Error is computed with respect to the value of T_T obtained numerically.

It can be seen from Table 2 that the homokinetic normal surface model best approximates the numerical data (Euler computations), with a relative error on T_T on the order of 1.0%. Furthermore, it is also interesting to notice that Froude's inlet model ($k^2K_1\to\infty$) yields a fairly good evaluation of T_T, within 1.3% of the numerical value. This can be related to the asymptotic evolution of T_T with respect to k^2K_1 [see Eq. (12)] which suggests that T_T is weakly dependent on k^2K_1 for sufficiently high values of k^2K_1. Conversely, both geometric and hemisphere models do not provide satisfactory results as they are not thoroughly consistent with one-dimensional assumptions. Subsequently, in what follows, the analytical approach will be assessed with respect to numerical data, for various viscous test cases, on the basis of the homokinetic inlet model.

D. Comparison of Analytical and Numerical Approaches

In the previous section, it has been shown that the analytical approach best approximates the numerical Euler computation when the homokinetic model is used. Here, in order to assess the robustness of the analytical model with respect to viscous effects, analytical results based on the homokinetic model are compared with numerical viscous (k-ϵ) computations for six test cases, corresponding to rotor thrusts roughly ranging from 0.5 to 3 N by steps of 0.5 N (Δp ranging from 20 to 120 Pa by steps of 20 Pa).

Table 3 shows that the analytical model is in good agreement with the numerical data, with a maximum error on T_T on the order of 8.2% at $Re=83489$ ($\Delta p=20$ Pa). Error is maximum at the lower Reynolds number due to the influence of viscous effects, which are not accounted for in the momentum balance formulation. On the other hand, it should be noticed that viscous effects have an influence on the analytical value of T_T via the inlet parameter k^2K_1. Here, the value of k^2K_1 is smaller than that obtained from non-viscous computations (see Table 2). In addition, it can be observed from Table 3 that k^2K_1 slightly decreases with the Reynolds number. However, these variations in k^2K_1 reflect only small changes in the velocity flow field at the shroud inlet (which is emphasized by the value of k squared), as comparison of Figs. 6b and 6d shows. Therefore, the influence of viscous effects via the inlet parameter k^2K_1 is of second-order with respect to that omitted in the momentum balance formulation.

To illustrate this feature, it can be shown that if k^2K_1 is fixed to 20 for all viscous cases, the maximum error on T_T is not drastically altered (8%). Furthermore, due to the asymptotic evolution of T_T with respect to k^2K_1, the maximum discrepancy does not exceed 12% if k^2K_1 tends to ∞.

Finally, although the result is independent on the inlet parameter, Table 3 shows that the value of P_i is analytically approximated within a maximum error of 3.8% with respect to viscous computations. As observed in Fig. 6, overestimation of analytical T_T and P_i principally arises from the absence of boundary layer modeling, which both generates viscous drag and mitigates the mass flow rate (see $\dot{m}$ in Table 3), as expected from the displacement effect.

E. Discussion

By definition, parameter k^2K_1 reflects the dependency of shroud performance on the two-dimensional flow field at the inlet of the

Table 3 Comparison of analytical values of $\dot{m}$, T_T and P_i for increasing Reynolds numbers

Re	Δp, Pa	T_R, N	$\dot{m}$, kg/s	k^2K_1	T_T, N	P_i, W
83489	20	0.51	0.21 (+3.8%)	21.27	1.17 (+8.2%)	3.45 (+3.8%)
118072	40	1.02	0.30 (+3.1%)	21.44	2.35 (+6.8%)	9.75 (+3.1%)
144608	60	1.53	0.37 (+2.7%)	21.52	3.52 (+6.2%)	17.92 (+2.7%)
166978	80	2.04	0.42 (+2.4%)	21.58	4.69 (+5.8%)	27.59 (+2.5%)
186688	100	2.54	0.47 (+2.3%)	21.64	5.87 (+6.7%)	38.55 (+2.3%)
204506	120	3.05	0.52 (+2.2%)	21.67	7.01 (+6.5%)	50.68 (+2.2%)
∞	120	3.05	0.52 (−1.2%)	25.99	7.08 (−1.0%)	50.68 (−1.2%)

Error with respect to the values obtained numerically are shown in round brackets.

shroud. Thus, it is rather intuitive that the value of k^2K_1 will, to some extent, depend on the design of the shroud. Nevertheless, the present section emphasizes the weak sensitivity of shroud performance to parameter k^2K_1 for suitable design that ensures large values of k^2K_1. Here, analytical results are compared with numerical viscous computations for three other test cases, corresponding to three distinct shroud geometries.

The geometries are displayed in Fig. 9. They have a similar rotor radius to that of the reference case previously addressed. Case A is a short shroud of length $L_S = 90$ mm and exit parameter $K_2 = 1.09$. Given the limited length of the nozzle, K_2 is reduced with respect to that of the reference case in order to avoid flow separation downstream the rotor. Case B has a similar nozzle to that of case A but exhibits an extended shroud lip, hence an increased shroud lip radius. The resulting shroud length is $L_S = 140$ mm. Case C has a similar exit parameter K_2 to that of the reference case but has shorter shroud lip and shroud nozzle, leading to $L_S = 120$ mm. For all three cases, the rotor thrust is set to 2.5 N ($\Delta p = 100$ Pa).

The analytical results are given in Table 4 for three values of k^2K_1. The first and third values are deduced from the homokinetic model and Froude's inlet model respectively, while the second value is the empirical value $k^2K_1 = 20$ proposed in the previous section.

Results reported in Table 4 provide evidence of the dependency of k^2K_1 on shroud geometry. These suggest that the analytical model could thus be enhanced through an empirical parameterization of k^2K_1 with respect to shroud design parameters (e.g. shroud lip radius, shroud length). Such parameterization would require more extensive numerical and/or experimental investigations, which goes beyond the scope of the present study. Nevertheless, as previously mentioned, Table 4 indicates that reasonable agreement between analytical and numerical values can be obtained using the empirical value $k^2K_1 = 20$, or even using 'Froude's approximation' $k^2K_1 \to \infty$. In other words, due to the relatively strong value of k^2K_1 and to the asymptotic evolution of T_T with respect to k^2K_1 [see Eq. (12)], results are only weakly affected by k^2K_1.

While the analytical model presented here can be used as a simple preliminary approach for the evaluation of shrouded rotor performance, it also suggests that k^2K_1 can be used as an indicator of the potential for shroud thrust improvement. Indeed, for a given outlet parameter K_2, larger k^2K_1 values are associated with larger T_T values, Froude's limit $k^2K_1 \to \infty$ being the asymptotic limit for shroud performance. Although the present study indicates that values on the order of $k^2K_1 = 20$ are a reasonable target, more extensive numerical and/or experimental investigations should be performed to complete the picture.

Table 4 Comparison of the analytical value of T_T for distinct values of k^2K_1

Case	k^2K_1	T_T, N	Error
A	17.49	5.38	+3.2%
	20	5.40	+3.6%
	∞	5.55	+6.5%
B	19.44	5.40	+2.1%
	20	5.40	+2.2%
	∞	5.55	+5.1%
C	20.22	5.86	+3.9%
	20	5.86	+3.8%
	∞	6.03	+7.0%

Error is computed with respect to the value of T_T obtained numerically.

IV. Conclusions

In this paper, Froude's theory is revisited in order to extract the aerodynamic characteristics of shrouded rotors. Due to the highly two-dimensional flow field induced at the lip of shrouded rotors, it is suggested that the analytical one-dimensional approach developed here be based on a homokinetic normal surface model. Such model ensures that the approach can reasonably be treated under one-dimensional assumptions.

Firstly, formulations for total, rotor, shroud, upstream shroud, and downstream shroud thrusts as well as induced power are derived, hence highlighting the role of specific system components in the global aerodynamics of shrouded rotors. It can be observed that, at given mass flow rate, while upstream shroud thrust is driven by inlet design parameter (k^2K_1), rotor and downstream shroud thrusts are driven by outlet parameter (K_2). In addition, the downstream shroud always generates drag and thus does not explicitly contribute to the generation of total thrust. Rather, the role of the downstream shroud (and of associated design parameter K_2) is to drive the mass flow rate, hence implicitly influencing the upstream shroud thrust. This implicit interplay between each system component indicates that the determination of optimal design criteria is not straightforward.

Secondly, the induced power is derived from previous relations and expressed as a function of the total thrust of the system. It is found that, at a given total thrust (which stands as an input parameter from the designer's perspective), the induced power admits a global minimum, which is a function of the outlet design parameter. Interestingly, the optimal outlet design parameter is directly linked to the inlet design parameter through the relation $K_2 = k^2K_1/2$, which

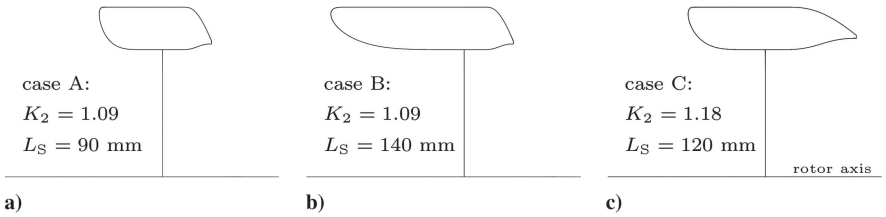

Fig. 9 Illustration of the three shroud geometries.

provides guidelines for the design of efficient shrouded rotors. In addition, this optimal criterion does not coincide with the cancellation of the drag of the downstream shroud (which is found to occur for $K_2 = 1$).

Subsequently, the analytical model is assessed with respect to results obtained from the resolution of the Navier–Stokes equations and its sensitivity to viscous effects is evaluated. Overall, the comparison between the analytical and numerical data shows good agreement, with a relative error on the total thrust on the order of 1% for potential flows and between 6 to 8% for low Reynolds number flows typical of micro air vehicles (MAVs). It is shown that for such low Reynolds number flows, both total thrust and induced power are slightly overestimated by the analytical model due to the absence of boundary layer modeling, which both generates viscous drag and mitigates mass flow rate.

Finally, the analytical model is tested on three distinct shroud geometries. It is indicated that while the inlet parameter k^2K_1 is geometry dependent, its variation with shroud design only weakly affects the analytical results. As such, it is shown that the empirical value $k^2K_1 = 20$ provides reasonable accuracy with respect to viscous computations. Nevertheless, it is suggested that the model could benefit from an empirical parameterization of k^2K_1 with respect to geometric parameters.

Appendix A: Extension of the Analytical Model to General Inflow Conditions

Here, total, rotor, and shroud thrust relations are reformulated for general inflow conditions, i.e. not restricted to hovering flight conditions. In what follows, V_∞ stands for the axial flight speed.

Total thrust:

$$T_T = \frac{1}{2}\rho A_R\left[\left(\frac{\dot{m}}{\rho A_R}\right)^2\left(\frac{2}{K_2} - \frac{1}{k^2K_1}\right) - k^2K_1V_\infty^2\right] \tag{A1}$$

Rotor thrust:

$$T_R = \frac{1}{2}\rho A_R\left[\left(\frac{\dot{m}}{\rho A_R}\right)^2\left(\frac{1}{K_2}\right)^2 - V_\infty^2\right] \tag{A2}$$

Shroud thrust:

$$T_S = \frac{1}{2}\rho A_R\left[\left(\frac{\dot{m}}{\rho A_R}\right)^2\left(\frac{2}{K_2} - \frac{1}{k^2K_1} - \frac{1}{K_2^2}\right) - (k^2K_1 - 1)V_\infty^2\right] \tag{A3}$$

Upstream shroud thrust:

$$T_{S_1} = \frac{1}{2}\rho A_R\left[\left(\frac{\dot{m}}{\rho A_R}\right)^2\left(1 - \frac{1}{k^2K_1}\right) - (k^2K_1 - 1)V_\infty^2\right] \tag{A4}$$

Downstream shroud thrust:

$$T_{S_2} = -\frac{1}{2}\rho A_R\left(\frac{\dot{m}}{\rho A_R}\right)^2\left(1 - \frac{1}{K_2}\right)^2 \tag{A5}$$

Appendix B: Alternative Derivation for Minimum Induced Power

Noting that the outlet design parameter K_2 drives the mass flow rate $\dot{m}$ of the system, a relation for the minimum induced power can be derived using $\partial P_i/\partial\dot{m} = 0$. Substituting Eq. (12) into Eq. (21)

$$\begin{aligned} P_i &= \frac{1}{2}\rho A_R\left(\frac{\dot{m}}{\rho A_R}\right)^3\left(\left(\frac{T_T}{\rho A_R}\right)\left(\frac{\dot{m}}{\rho A_R}\right)^{-2} + \frac{1}{2k^2K_1}\right)^2 \\ &= \frac{1}{2}\rho A_R\left(\left(\frac{T_T}{\rho A_R}\right)^2\left(\frac{\dot{m}}{\rho A_R}\right)^{-1} + \frac{1}{4k^4K_1^2}\left(\frac{\dot{m}}{\rho A_R}\right)^3\right. \\ &\quad \left. + \frac{T_T}{\rho A_R k^2K_1}\left(\frac{\dot{m}}{\rho A_R}\right)\right) \end{aligned} \tag{B1}$$

hence

$$\begin{aligned} \frac{\partial P_i}{\partial\dot{m}} = \frac{1}{2}\rho A_R\left(-\left(\frac{T_T}{\rho A_R}\right)^2\rho A_R\dot{m}^{-2}\right. \\ \left. + \frac{3}{4k^4K_1^2\left(\rho A_R\right)^3}\dot{m}^2 + \frac{T_T}{(\rho A_R)^2k^2K_1}\right) \end{aligned} \tag{B2}$$

Subsequently, writing the following equivalence

$$\frac{\partial P_i}{\partial\dot{m}} = 0 \Leftrightarrow \frac{2\dot{m}^2}{\rho A_R}\frac{\partial P_i}{\partial\dot{m}} = 0 \tag{B3}$$

and solving for the roots of the quadratic equation

$$\frac{3}{4k^4K_1^2(\rho A_R)^3}\dot{M}^2 + \frac{T_T}{(\rho A_R)^2k^2K_1}\dot{M} - \left(\frac{T_T}{\rho A_R}\right)^2\rho A_R = 0 \tag{B4}$$

where $\dot{M} = \dot{m}^2$, the optimum mass flow rate can be obtained

$$\dot{m}_{\text{opt}}^2 = \frac{2}{3}\rho A_R k^2K_1T_T \tag{B5}$$

Finally, substituting $\dot{m}_{\text{opt}}$ into Eq. (12) yields

$$T_T = \rho A_R\frac{2\rho A_R K_1T_T}{3(\rho A_R)^2}\left(\frac{1}{K_2} - \frac{1}{2k^2K_1}\right) \tag{B6}$$

which suggests an optimum value for the outlet design parameter K_2

$$K_2 = \frac{k^2K_1}{2} \tag{B7}$$

While the K_2 parameter is used as a geometric design variable to optimize the system, it is interesting to note that thrust enhancement is linked to increased mass flow rate which promotes shroud lip suction.

References

[1] Mueller, T. J., and DeLaurier, J. D., "Aerodynamics of Small Vehicles," *Annual Review of Fluid Mechanics*, Vol. 35, No. 1, 2003, pp. 89–111. doi:10.1146/annurev.fluid.35.101101.161102

[2] Torres, G. E., and Mueller, T. J., "Low Aspect Ratio Aerodynamics at Low Reynolds Numbers," *AIAA Journal*, Vol. 42, No. 5, 2004, pp. 865–873. doi:10.2514/1.439

[3] Pines, D. J., and Bohorquez, F., "Challenges Facing Future Micro-Air-Vehicle Development," *Journal of Aircraft*, Vol. 43, No. 2, 2006, pp. 290–305. doi:10.2514/1.4922

[4] Dickinson, M. H., Lehmann, F. O., and Sane, S. P., "Wing Rotation and the Aerodynamic Basis of Insect Flight," *Science*, Vol. 284, No. 5422, 1999, pp. 1954–1960. doi:10.1126/science.284.5422.1954

[5] Platzer, M. F., Jones, K. D., Young, J., and Lai, J. C. S., "Flapping Wing Aerodynamics: Progress and Challenges," *AIAA Journal*, Vol. 46, No. 9, 2008, pp. 2136–2149. doi:10.2514/1.29263

[6] Shyy, W., Aono, H., Chimakurthi, S. K., Trizila, P., Kang, C. K., Cesnik, C. E. S., and Liu, H., "Recent Progress in Flapping Wing Aerodynamics and Aeroelasticity," *Progress in Aerospace Sciences*, Vol. 46, No. 7, 2010, pp. 284–327. doi:10.1016/j.paerosci.2010.01.001

[7] Jardin, T., Farcy, A., and David, L., "Three Dimensional Effects in Hovering Flapping Flight," *Journal of Fluid Mechanics*, Vol. 702, July 2012, pp. 102–125. doi:10.1017/jfm.2012.163

[8] Lipera, L., Colbourne, J. D., Tischler, M. B., Mansur, M. H., Rotkowitz, M. C., and Patangui, P., "The Micro Craft iSTAR Micro Air Vehicle: Control System Design and Testing," *Annual Forum Proceedings–American Helicopter Society*, Vol. 57, AHS International, Alexandria, VA, 2001, pp. 1998–2008.

[9] Pereira, J. L., and Chopra, I., "Hover Tests of Micro Aerial Vehicle Scale Shrouded Rotors, Part I: Performance Characteristics," *Journal of the American Helicopter Society*, Vol. 54, No. 1, 2009, p. 12001. doi:10.4050/JAHS.54.012001

[10] Pereira, J. L., and Chopra, I., "Hover Tests of Micro Aerial Vehicle Scale Shrouded Rotors, Part II: Flow Field Measurements," *Journal of the American Helicopter Society*, Vol. 54, No. 1, 2009, Paper 12002. doi:10.4050/JAHS.54.012002

[11] Lakshminarayan, V. K., and Baeder, J. D., "Computational Investigation of Microscale Shrouded Rotor Aerodynamics in Hover," *Journal of the American Helicopter Society*, Vol. 56, No. 4, 2011, Paper 042002. doi:10.4050/JAHS.56.042002

[12] Lee, T. E., Leishman, J. G., and Rand, O., "Design and Testing of a Ducted Coaxial Rotor System for Application to a Micro Aerial Vehicle," *Annual Forum Proceedings–American Helicopter Society*, Vol. 66, AHS International, Alexandria, VA, 2010, pp. 1404–1425.

[13] Hrishikeshavan, V., and Chopra, I., "Performance, Flight Testing of Shrouded Rotor Micro Air Vehicle in Edgewise Gusts," *Journal of the American Helicopter Society*, Vol. 49, No. 1, 2012, pp. 193–205. doi:10.2514/1.C031477

[14] Horlock, J. H., *Actuator Disk Theory*, McGraw Hill, New York, 1978.

[15] Rosen, A., and Gur, O., "Novel Approach to Axisymmetric Actuator Disk Modelling," *AIAA Journal*, Vol. 46, No. 11, 2008, pp. 2914–2925. doi:10.2514/1.37383

[16] Huo, C., Barènes, R., Gressier, J., and Grondin, G., "Numerical Study on Parametrical Design of Long Shrouded Contra-Rotating Propulsion System in Hovering," *World Academy of Science, Engineering and Technology*, Vol. 5, 2011, pp. 1963–1972.

[17] Huo, C., "Experimental and Numerical Analysis of a Shrouded Contrarotating Coaxial Rotor in Hover," Ph.D. Dissertation, Aerodynamics, Energetics and Propulsion Dept., Univ. of Toulouse, Toulouse, France, 2012.

[18] Quartapelle, L., and Napolitano, M., "Force and Moments in Incompressible Flows," *AIAA Journal*, Vol. 21, No. 6, 1983, pp. 911–913. doi:10.2514/3.8171

[19] Noca, F., Shiels, D., and Jeon, D., "A Comparison of Methods for Evaluating Time-Dependent Fluid Dynamic Forces on Bodies, Using Only Velocity Fields and Their Derivatives," *Journal of Fluids and Structures*, Vol. 13, No. 5, 1999, pp. 551–578. doi:10.1006/jfls.1999.0219

[20] David, L., Jardin, T., and Farcy, A., "On the Non-Intrusive Evaluation of Fluid Forces with the Momentum Equation Approach," *Measurement Science and Technology*, Vol. 20, No. 9, 2009, Paper 095401. doi:10.1088/0957-0233/20/9/095401

[21] Moschetta, J. M., "Explo-Drone: Autonomous Exploration of Confined Environments by Compact Micro Air Vehicles," Actions Thématiques Stratégiques de l'Université de Toulouse, Toulouse, France, 2013.

[22] Dyer, K., "Aerodynamic Study of a Small, Ducted VTOL Aerial Vehicle," M.Sc. Dissertation, Aeronautics and Astronautics Dept., Massachusetts Institute of Technology, Cambridge, MA, 2002.

[23] Pereira, J. L., and Chopra, I., "Effects of Shroud Design Variables on Hover Performance of a Shrouded-Rotor for Micro Air Vehicle Applications," *Specialists' Meeting Proceedings–American Helicopter Society*, AHS International, Alexandria, VA, 2005.

Z. Rusak
Associate Editor